

Energy Technology & Environmental Science

Atomically Precise Noble Metal Clusters Harvest Visible Light to Produce Energy

V. Jeseentharani,^[a] N. Pugazhenthiran,^[a] Ammu Mathew,^[a] Indranath Chakraborty,^[a] Ananya Bakshi,^[a] Jyotirmoy Ghosh,^[a] Madhuri Jash,^[a] G. S. Anjusree,^[b] T. G. Deepak,^[b] A. Sreekumaran Nair,^{*[b]} and T. Pradeep^{*[a]}

Atomically precise gold and silver clusters are a new class of sensitizers which can be used as substitutes for dyes in the classical dye-sensitized solar cells (DSCs). Here noble metal clusters protected by proteins and thiols (Au₃₀@BSA, Au₂₅SBB₁₈, and Ag₄₄MBA₃₀) have been used for photovoltaic studies. These metal clusters were used as sensitizers for the photoanodes fabricated using TiO₂ nanotubes (NTs) and the commercial P25

TiO₂ nanoparticles. The TiO₂ clusters and the solar cells were characterized by spectroscopy, microscopy, current-voltage (*I-V*) and incident photon-to-current conversion efficiency (IPCE) measurements. A systematic *I-V* study revealed a conversion efficiency of 0.35 % for the Au₃₀@BSA sensitized solar cell made from TiO₂ NTs which showed an IPCE maximum of 3 % at ~ 400 nm.

Introduction

Quantum clusters (QCs) are a new class of sub-nanometer sized materials, comprising of a few atoms protected by proteins or organic thiols and they are represented simply using their metal cores, such as Au₈, Au₁₁, Au₁₃ or Au₂₅.^[1] These QCs have possible applications in single molecule spectroscopy, biological labeling,^[2-4] sensing,^[5-8] catalysis,^[9-15] and other fields.^[16-19] Amongst the various clusters synthesized so far by different methods, some are extremely stable at room temperature. The high stability of bovine serum albumin (BSA) protected gold cluster (Au₃₀BSA) is attributed to the complete protection of Au by proteins. In comparison, the stability of thiol-protected clusters is often associated to their closed shell electronic structure composed of *n* electrons (*n* = 2, 8, 18, 34, 58, 92, ...).^[20]

Quantum clusters have remarkable optical and electronic properties.^[21-24] They possess discrete energy states and exhibit characteristic luminescence. The luminescence of these atomically precise clusters has been found to be sensitive to many factors such as chemical contamination, pH, temperature, etc. Anchoring QCs on mesoscale particles leads to surface enhancement of their luminescence. The Au₂₅@BSA and

Ag₁₅@BSA clusters display distinct features in their emission spectrum. The Ag₁₅@BSA cluster has been demonstrated as a sensor for TNT (2,4,6-trinitrotoluene) and Hg²⁺ ions by quenching of cluster luminescence. These studies have been performed at a single particle level.^[25] Ultra-trace Hg²⁺ detection at 10⁻²¹ mole level using atomically precise Au@BSA clusters coated on single nanofibers was demonstrated.^[26] Quenching of the red emission upon exposure to mercury has been observed under a dark field fluorescence microscope.^[26] Many other researchers have also looked at the use of Au@BSA clusters in sensor applications.^[27,28]

In a dye/quantum dot (QD)-sensitized solar cell (DSC/QDSC), the dye or QD functions as a source of photoelectrons.^[29] The photoexcited electrons are injected into the conduction band of the semiconductor from the lowest unoccupied molecular orbital (LUMO) of the dye or the conduction band of the QD. The semiconductor employed is often nano titanium dioxide (TiO₂). The electrons are transported through TiO₂ arrays in the photoelectrode to the back contact [usually a transparent conducting oxide such as fluorine-doped tin oxide (FTO) on glass]. The oxidized dye/QD is regenerated using a redox electrolyte, which in turn is brought back to the original state by the electrons from the counter electrode. Several factors such as crystallinity, morphology, porosity of TiO₂, absorption characteristics of the sensitizer, etc. play important roles in determining the overall efficiency of the solar cells.

TiO₂ is the preferred metal oxide for DSCs due to its desired surface chemistry, abundance, low-cost, environment friendliness, and favorable alignment of its conduction band edge with the LUMO/CB of the dyes/QDs, etc. The conventional DSCs use Ru-based metal-organic dyes (N3, N719, and Black dye) for sensitization. Ru being a rare metal (rarer than gold), the Ru-based dyes are expensive.^[30,31] Therefore, search for non-Ru based dyes is essential for the success of DSCs. Amongst the

[a] Dr. V. Jeseentharani, Dr. N. Pugazhenthiran, Dr. A. Mathew, Dr. I. Chakraborty, Dr. A. Bakshi, J. Ghosh, M. Jash, Prof. T. Pradeep
DST Unit of Nanoscience (DST UNS) and Thematic Unit of Excellence
Department of Chemistry
Indian Institute of Technology Madras
Chennai 600036, India
E-mail: pradeep@iitm.ac.in

[b] G. S. Anjusree, T. G. Deepak, Dr. A. S. Nair
Amrita Centre for Nanosciences and Molecular Medicine
Amrita Institute of Medical Sciences (AIMS)
Ponekkara, AIMS PO, Kochi 682041, India
E-mail: sreekumarannair@aims.amrita.edu

Supporting information for this article is available on the WWW under <http://dx.doi.org/10.1002/slct.201601730>

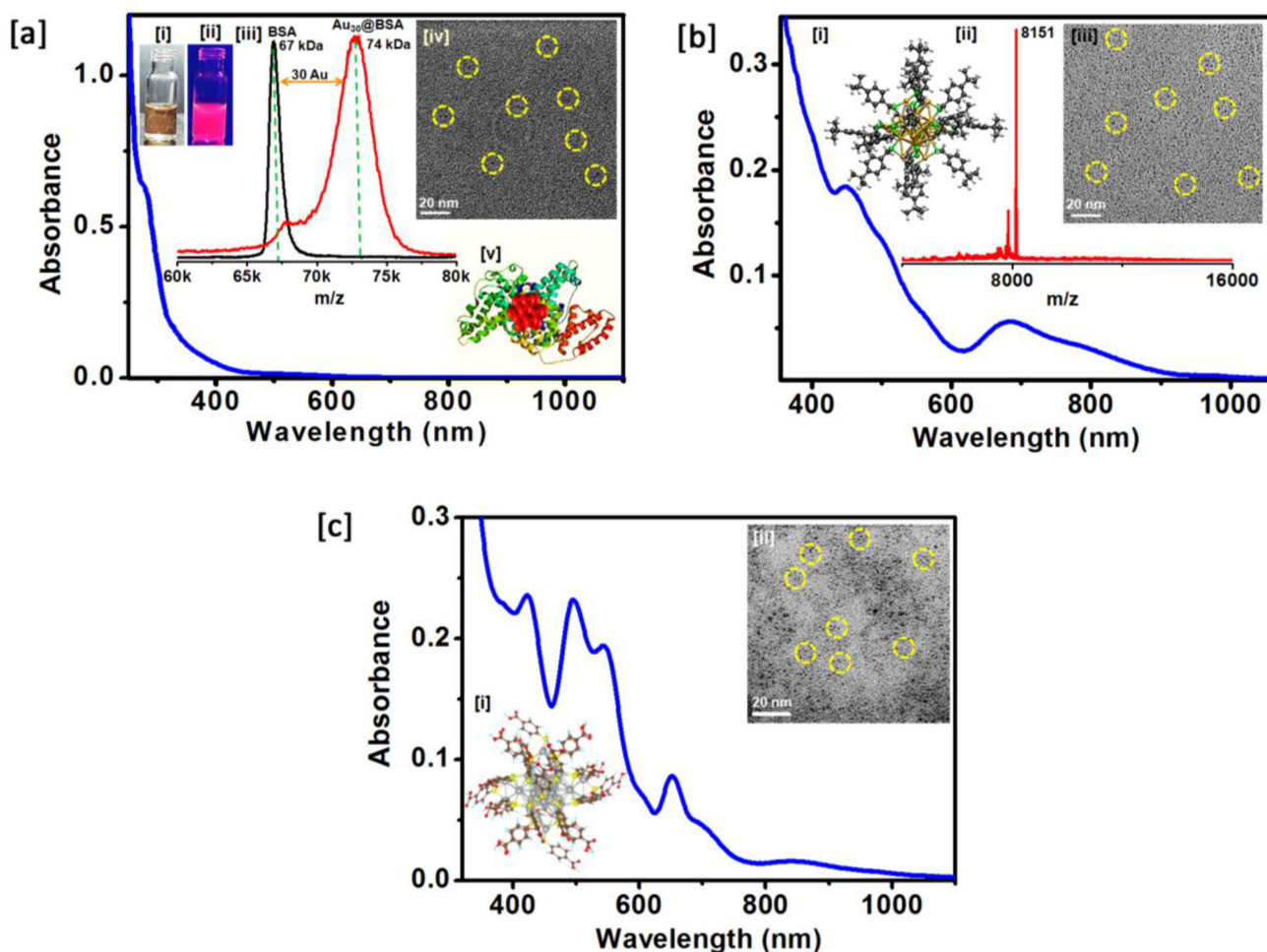


Figure 1. [a] UV-Vis absorption spectrum of $\text{Au}_{30}\text{@BSA}$ cluster in water. Insets show the photographs of clusters in water illuminated with visible (i) and UV light (ii); MALDI-MS spectrum of $\text{Au}_{30}\text{@BSA}$ shows a sharp peak at m/z 73,000 in the positive mode (iii); TEM image of $\text{Au}_{30}\text{@BSA}$ cluster (iv); graphical representation of $\text{Au}_{30}\text{@BSA}$ structure (v); [b] UV-vis absorption spectra of $\text{Au}_{25}\text{SBB}_{18}$; inset shows the structure of $\text{Au}_{25}\text{SBB}_{18}$ (i)^[54]; MALDI (linear) mass spectra in the positive ion mode (B) of $\text{Au}_{25}\text{SBB}_{18}$ (ii). The peak at m/z 8151 is due to $\text{Au}_{25}\text{SBB}_{18}$; TEM image of $\text{Au}_{25}\text{SBB}_{18}$; [c] UV-vis absorption spectra of $\text{Ag}_{44}\text{MBA}_{30}$; inset shows the structural representation of $\text{Ag}_{44}\text{MBA}_{30}$ (i) and TEM image of $\text{Ag}_{44}\text{MBA}_{30}$ cluster. The yellow circles in the TEM images represent the quantum clusters.

non-Ru based dyes for DSCs,^[32-36] the porphyrine-based ones were found to be ideal.^[37-39] QCs can be utilized as substitutes for the dyes in DSCs as they also have the potential for absorbing light in the visible region and show high stability to visible and infrared light.^[40-45] The plasmonic effect of noble metals can help in the enhancement in the performance of solar cells.^[46,47]

In the present work, the usefulness of the BSA (bovine serum albumin), SBB (4-(*t*-butyl)benzylmercaptan) and MBA (4-mercaptobenzoic acid)-protected gold and silver QCs as sensitizers for solar cells has been compared. While there have been a few reports of cluster-based DSSCs, they have used only glutathione protected systems.^[41,48,49] A comparison of various QCs with varying ligands is essential as glutathione protected clusters are generally unstable especially in presence of electrolytes. Protecting ligands are important for proper linkages with TiO_2 as well as for imparting stability to the cluster systems. The TiO_2 nanotubes (NTs) employed as the photoanode were synthesized by the hydrothermal method. Amongst the low

temperature methods, the hydrothermal/solvothermal method is a versatile route for the synthesis of nanomaterials.^[50]

Experimental

Synthesis and characterization of the $\text{Au}_{30}\text{@BSA}$, $\text{Au}_{25}\text{SBB}_{18}$ and $\text{Ag}_{44}\text{MBA}_{30}$ quantum clusters, TiO_2 nanotubes and the solar cell fabrication methodology are discussed in detail in the Supporting Information 1 (SI-1).

Results and Discussion

The characteristic properties of the synthesized $\text{Au}_{30}\text{@BSA}$, $\text{Au}_{25}\text{SBB}_{18}$ and $\text{Ag}_{44}\text{MBA}_{30}$ clusters are shown in Figure 1. In view of their reported properties, we present only the essential aspects here. The synthesized $\text{Au}_{30}\text{@BSA}$ clusters did not show any distinct absorption feature in the visible region, though a characteristic onset of absorption was observable at 520 nm (Figure 1a). $\text{Au}_{30}\text{@BSA}$ is a water soluble luminescent cluster

exhibiting bright red emission at 680 nm when excited at 365 nm at room temperature (Figure S1 in supporting information (SI)). Photographs of the brown-colored cluster solution under visible light and UV light are shown as insets (i) and (ii) in Figure 1a. Mass spectra of the protein and the cluster were measured by MALDI-TOF-MS using sinapinic acid as the matrix. The spectra were collected in the positive ion mode. BSA shows a distinct peak at 67 kDa in agreement with the literature (Figure 1a).^[51] For Au₃₀@BSA, the major peak is positioned at m/z 74 kDa. The difference between the above two peaks corresponds to Au₃₀, which suggests that the cluster is fully encapsulated by a single protein molecule. HRTEM images also show the presence of sub-nanometer sized clusters of Au₃₀@BSA (Figure 1a (iv)) as dark spots highlighted as broken circles in yellow color. HR-TEM image of a single cluster is not possible in an isolated state because the sub-nano clusters (~0.8 nm) are prone to electron beam-induced aggregation.^[52-56] A graphical representation of Au₃₀@BSA is shown in Figure 1a (v). In contrast to Au₃₀@BSA, the thiolate-protected gold cluster (Au₂₅SBB₁₈) has a well-defined optical absorption spectrum as shown in Figure 1b, revealing discrete molecule-like features which are characteristic of Au₂₅ QCs. Absorption spectra of the quantum clusters of Au₂₅SBB₁₈ show peaks at 448 nm and 683 nm, respectively. The peak at 448 nm has ligand-metal (SBB-Au₂₅) character.^[57] The absorption at 683 nm is due to the intra-band transition derived from sp orbitals of Au. This peak is characteristic of the Au₂₅ clusters and occurs in all spectra of Au₂₅ clusters reported in the literature.^[58,59] The structure of Au₂₅SBB₁₈ is shown in Figure 1b (i).^[54,60] The cluster was confirmed by MALDI MS shown in Figure 1b (ii). DCTB (trans-2-[3-(4-t-butylphenyl)-2-methyl-2-propenylidene] malononitrile) was used as the matrix for MALDI MS measurements of Au₂₅SBB₁₈. An intact molecular ion peak observed at m/z 8151 in Figure 1b (ii) confirms that the cluster is Au₂₅SBB₁₈ and its high intensity is indicative of the purity of the prepared cluster.

The average size of the cluster was determined to be less than 2 nm from TEM (Figure 1b (iii)). Interestingly, the clusters did not show any significant electron-beam-induced aggregation, a common phenomenon observed in other Ag and Au clusters.^[60] This may be due to the enhanced stability provided by the bulky ligand shell around the cluster. The Au₃₀@BSA clusters appeared monodisperse and the average size of the clusters was 0.8 nm. The inset of Figure 1c (ii) shows the HRTEM image of Ag₄₄MBA₃₀ whose core size was found to be 1.2 nm. A histogram showing size distribution of Ag₄₄MBA₃₀ is shown in the SI (Figure S3). For Au₂₅SBB₁₈ clusters, the average size was >2 nm as confirmed by TEM and it did not show any electron beam-induced aggregation. The optical absorption spectrum of Ag₄₄MBA₃₀ shows several peaks in the 300-1000 nm region (Figure 1c). Five intense bands at 850, 651, 545, 496 and 423 nm, respectively, have been observed along with three broad bands centered at around 703, 608 and 386 nm. These characteristic bands confirm the purity of the cluster.^[61] The prominent peak at 850 nm is plotted in energy scale^[62] and shown in Figure S2. The structure of Ag₄₄MBA₃₀ is shown in Figure 1c (i). All the characterization data show that a highly

homogenous cluster has been used for the preparation solar cells.

The X-ray diffraction (XRD) pattern of the TiO₂ NTs is shown in Figure 2a. The peaks in the XRD were indexed corresponding

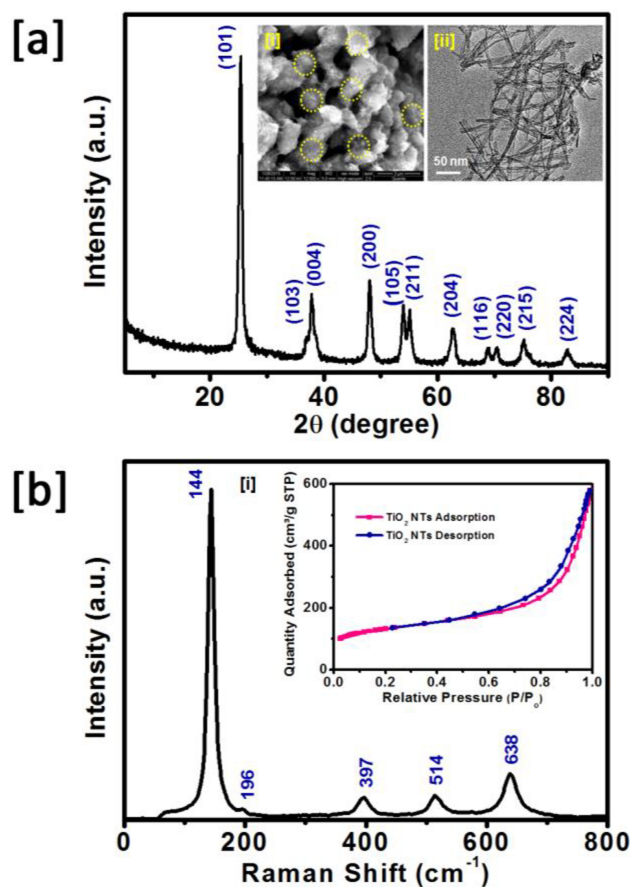


Figure 2. [a] Powder XRD spectrum of synthesized TiO₂NTs; Insets show the SEM morphology of TiO₂NTs in which agglomerated tubes are seen (circled) (i) and TEM image of TiO₂NTs (ii); [b] Raman spectra of the anatase TiO₂NTs; Inset shows the nitrogen adsorption–desorption isotherms of TiO₂NTs.

to the standard database, JCPDS No. 21-1272. The most intense diffraction peak observed at 2θ value of 25.43° corresponds to the (101) plane of anatase TiO₂. The average crystallite size of the TiO₂ NTs calculated from the Debye-Scherrer formula:

$$L = 0.89\lambda / \beta \cos\theta \quad (1)$$

[where L is the average particle size, λ is the X-ray wavelength, β is the full width at half maximum (FWHM) and θ is the Bragg's angle] was 11.71 nm, which is in close agreement with the TEM results. The synthesized TiO₂ was characterized by spectroscopy and microscopy. The surface morphology of the hydrothermally prepared TiO₂ NTs was examined by SEM analysis. It can be seen in Figure 2a (i) that the TiO₂ NTs are uniformly distributed. The TEM images (Figure 2a (ii)) illustrate the TiO₂ NTs produced were well shaped and randomly oriented. TEM analysis also

yielded the diameter and length of the TiO₂ NTs with an internal cavity of 10 - 12 nm and 200 - 250 nm, respectively. In the Raman spectrum (Figure 2b) of TiO₂, the peaks centered at 144, 196 and 638 cm⁻¹ denote the E_g Raman modes and that at 397 and 514 cm⁻¹ represent B_{1g} and A_{1g} Raman modes, respectively, of anatase TiO₂.^[63,64]

No other peaks characteristic of any other form of TiO₂ (say rutile for example) were observed either in the XRD or in the Raman spectrum, indicating the phase purity of the prepared TiO₂ NTs. The nitrogen adsorption-desorption isotherms of the TiO₂ NTs are depicted in the inset Figure 2b (i). The Brunauer-Emmett-Teller (BET) surface area of the TiO₂ NTs was zestimated to be 469 m²/g, which is higher than that of the commercially available P25 TiO₂ (~40 m²/g).^[65] The Barrett-Joyner-Halenda (BJH) pore volume and pore size of the TiO₂ NTs were found to be 0.896 cm³/g and 9 nm, respectively indicating the mesoporosity of the TiO₂. X-ray photoelectron spectroscopy (XPS) was carried out to examine the phase purity and oxidation state of Ti in TiO₂ (see SI, Figure S4). The XPS spectra confirm the existence of Ti in its Ti⁴⁺ state based on the presence of the two peaks located at 458.8 eV and 465.3 eV, corresponding to 2p_{3/2} and 2p_{1/2} of Ti⁴⁺, respectively. The O1s peak at a binding energy of 530.7 eV is attributed to O²⁻. The XPS analysis also confirmed the absence of impurities in the synthesized TiO₂ NTs.^[66] SEM and XRD were also used to characterize commercial P25 (see SI, Figure S5). XRD showcased the co-existence of rutile and anatase phases in P25 versus pure anatase phase in the TiO₂ NTs.

The TiO₂ NTs and P25 electrodes prepared by doctor-blading (and subsequent sintering at 450°C) were immersed into the cluster solutions. For comparative studies, two different thicknesses of TiO₂ NT and P25 TiO₂ (12 and 18 μm, respectively) were used. In this study, we fabricated the quantum cluster-sensitized solar cell (QCSSC) by applying the same processing conditions as for DSSCs; in the former, quantum cluster substitutes the dye. The experimental details can be found in SI.

The Au₃₀@BSA modified TiO₂ NT was further characterized via TEM, XPS and Raman spectroscopy to confirm the presence of Au QCs on the TiO₂ NT surface. The increase in weight was observed after immersion of the TiO₂ electrode into the Au₃₀@BSA cluster solution. TEM analysis showed that the clusters were coated onto the surface of the TiO₂ electrode (see SI, Figure S6). This was confirmed from the EDS data shown in Figure S6 (clusters and TiO₂ are labeled). XPS analysis was carried out to examine the elemental composition of Au₃₀@BSA-modified TiO₂ photoanode and to identify the oxidation state of Au in TiO₂ doped Au cluster shown in Figure 3(a-d). The fully scanned survey spectrum of Au modified TiO₂ is shown in Figure 3a which shows Au, Ti, O, N and C. The XPS spectrum displayed the characteristic peak of Au showing nearly zero oxidation state. The 4f core-level photoemission spectrum of Au₃₀@BSA is expanded in Figure 3b. The BE of Au⁰4f_{7/2} of the gold QCs comes in between 84 and 86 eV.^[61] Two components due to Au⁰ (84.5 eV for 4f_{7/2} and 88.2 eV for 4f_{5/2}) and Au¹⁺ (86.1 and 89.7 eV) are used to fit the spectrum. Most of the intensity is due to Au⁰ and the Au¹⁺

components are assumed to be due to the protein bound surface atoms of the cluster.

From Figure 3c, the spin-orbit split components (2p_{3/2} and 2p_{1/2}) of the Ti 2p peak were de-convoluted into two components centered at 458.5 and 464.1 eV. The measured separation between the Ti 2p_{3/2} and Ti 2p_{1/2} peaks was 5.6 eV, which is consistent with the binding energy separation observed for stoichiometric TiO₂. The O1s peak of Au modified TiO₂ on the surface could be fitted to three Gaussian curves centered at ~530.8, ~532.6, and ~533.9 eV, respectively shown in Figure 3d. The OI species at the low binding energy of 530.8 eV belongs to O²⁻ ions in the anatase TiO₂ structure.^[67-69] The OII species with a medium binding energy centered around 532.6 eV is attributed to O⁻ and O²⁻ ions in the oxygen deficient region mainly caused by oxygen vacancies.^[70] The high binding energy species, OIII centered at ~533.9 eV belong to the absorbed or dissociated oxygen or OH species on the surface of TiO₂.^[71] The sample was finally analyzed by Raman spectroscopy (Figure S7). The anatase phase of the TiO₂ matrix was observed along with the luminescent feature of the cluster, around 2644.3 cm⁻¹ (619 nm); note that the sample was excited using 532 nm laser.

Figure 4a shows a schematic representation of occupied and unoccupied electronic energy levels near the Fermi level, E_F. E_{vac} is the vacuum level at which the energy of the electron is zero. E_{CBM} and E_{VBM} are the conduction-band minimum and the valance band maximum, respectively. Other abbreviations are: E_g - energy gap, IP - ionization potential and EA - electron affinity. Figure 4(b-d) show the typical He1 UPS spectra of standard Au₃₀BSA, Au₂₅SBB₁₈ and Ag₄₄MBA₃₀, respectively. The location of the Fermi level relative to the vacuum level, E_{vac} - E_F, can be determined using the following relation:^[71,72]

$$hv = |E_{\text{cutoff}}| + E_{\text{vac}} - E_{\text{F}} \quad (2)$$

where |E_{cutoff}| is the location of the inelastic cutoff and hv is the incident photon energy of 21.21 eV. The work function of Ag is 4.26 eV. From the UPS spectrum, E_{cutoff} of standard Ag is 16.95 eV (Figure S8). The |E_{cutoff}| of Au₃₀BSA, Au₂₅SBB₁₈ and Ag₄₄MBA₃₀, are 16.27, 16.45 and 16.18 eV, respectively as indicated in Figure 4(b-d). From this E_{vac} - E_F was calculated and the values for Au₃₀BSA, Au₂₅SBB₁₈ and Ag₄₄MBA₃₀ are 4.94, 4.76 and 5.03 eV, respectively. The ionization potential (IP) is the location of the valance-band maximum (VBM), E_{VBM}, relative to E_{vac}. E_{VBM} can be determined by choosing the point of maximum inflection near E_F as indicated in Figure 4(b-d), and the E_F - E_{VBM} were 1.52, 1.67 and 1.45 eV and IP values (equivalent to the HOMO level of the clusters) were calculated to be 6.46, 6.43 and 6.48 eV for Au₃₀BSA, Au₂₅SBB₁₈ and Ag₄₄MBA₃₀, respectively. The inset of Figure 4c showed the point of inflection of Au₂₅SBB₁₈. Since UPS only probes occupied states, conduction band minimum (CBM) cannot be determined from the UPS measurements.

However, the E_{CBM} values were estimated knowing the IP values (described above) and the optical band-gap, E_g determined from UV-Vis measurements. These were 1.65, 1.33 and 1.18 eV for Au₃₀BSA, Au₂₅SBB₁₈ and Ag₄₄MBA₃₀, respectively.

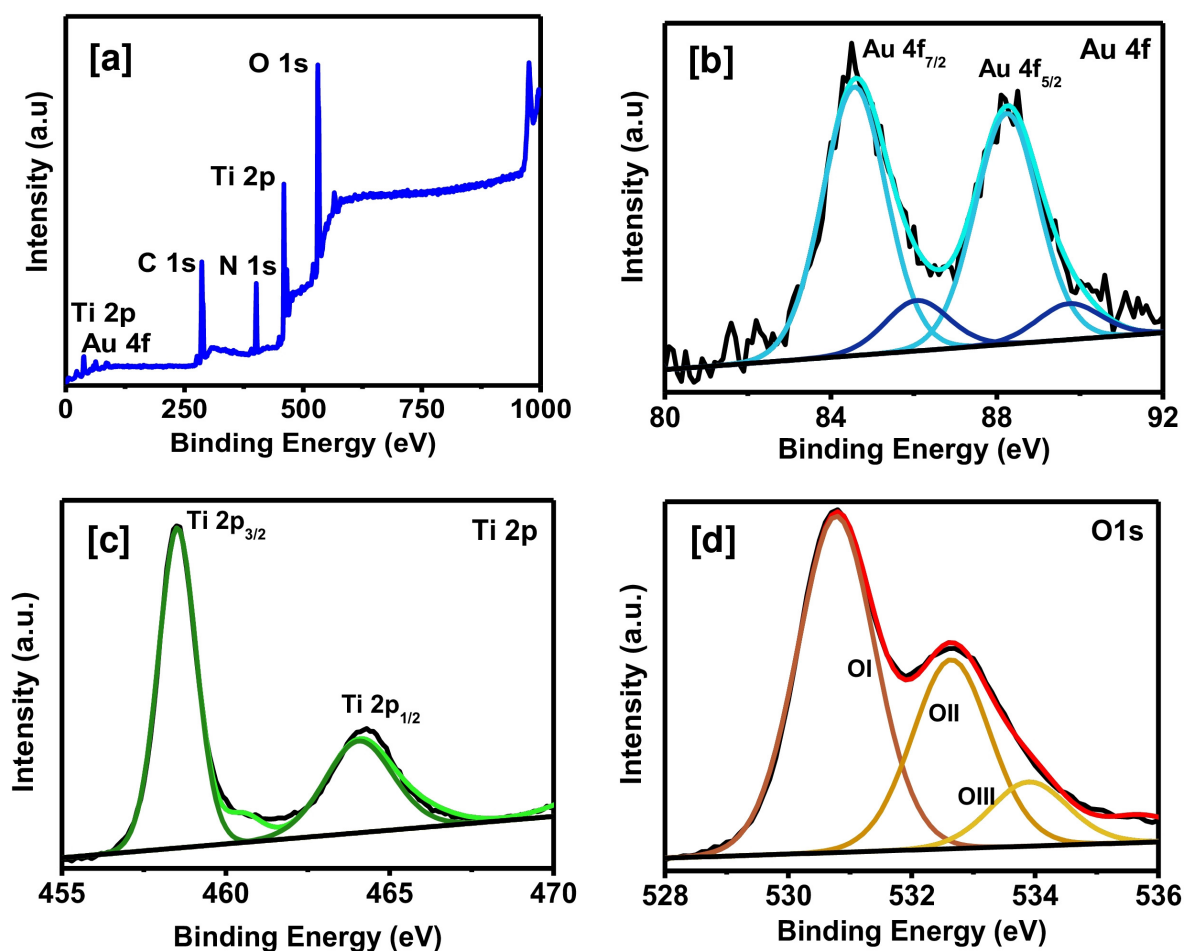


Figure 3. [a] Survey spectrum of Au₃₀@BSA modified TiO₂ NT; Expanded XPS spectra of [b] Au 4f, [c] Ti 2p and [d] O 1s.

Thus calculated EA values were found to be 4.81, 5.10 and 5.30 eV, respectively, with respect to the vacuum level. Thus it can be summarized that the values of E_{HOMO} of the clusters are -6.46, -6.43 and -6.48 eV and that of E_{LUMO} are -4.81, -5.10 and -5.30 eV, respectively. A schematic and the energy level diagram of the quantum cluster-sensitized solar cell can be depicted as in Figure 5a and 5b, respectively. A schematic and the energy level diagram of the quantum cluster-sensitized solar cell can be depicted as in Figure 5a and 5b, respectively.

The redox potential of the cobalt electrolyte, $[\text{Co}(\text{bpy})_3]^{3+} \rightarrow [\text{Co}(\text{bpy})_3]^{2+}$ and the band-gap of anatase TiO₂ were taken from literature.^[73,74] The positions of the valence and conduction bands of TiO₂ were determined using ultraviolet photo-emission spectroscopy and the band-gap was taken as 3.2 eV.^[70] The current density-voltage (J - V) curves for Au₂₅SBB₁₈, Au₃₀@BSA and Ag₄₄MBA₃₀ QCSSCs fabricated with 12 and 18 μm thick TiO₂ NTs and P25 TiO₂, respectively, are shown in Figure 6(a-c). Note that in all systems, saturation coverage of the cluster was used. The energy conversion efficiency (η) was calculated from the short-circuit current (J_{sc}), open-circuit voltage (V_{oc}), fill-factor (FF) (obtained from the I - V measurements) and intensity of the incident light (P_{in}) according to the formula:

$$\eta = \frac{[J_{\text{sc}}(\text{mA}\cdot\text{cm}^{-2})][V_{\text{oc}}(\text{V})][\text{FF}]}{P_{\text{in}}(\text{mW}\cdot\text{cm}^{-2})} \quad (3)$$

The values of the V_{oc} , J_{sc} , FF and η are summarized in Table 1. The redox electrolyte employed was Co³⁺/Co²⁺ redox couple. The traditional I₃⁻/I⁻ redox electrolyte was not used because the cluster cores were prone to oxidation by I⁻. A comparison of the photovoltaic parameters implies that solar cells with Au₃₀@BSA as the sensitizer showed the highest energy conversion efficiencies (0.17-0.35%) amongst the three. The Au₃₀@BSA on 18 μm thick P25 TiO₂ and 18 μm thick TiO₂NT electrodes showed an efficiency of 0.30% and 0.35%, respectively. This enhancement is due to an increase in the photovoltaic parameters namely: V_{oc} and J_{sc} compared to the other systems. The Au₃₀@BSA-modified 18 μm thick TiO₂ NT solar cell exhibited a photocurrent of 0.98 mA/cm² and an open-circuit voltage of 0.71 V, as opposed to a low photo response obtained (0.17 mA/cm² of photocurrent and 0.33 V of open-circuit voltage) in the absence of the Au₃₀@BSA sensitizer (SI, Figure S9). This implies that the enhanced photocurrent observed in the case is due to the sensitizing property of the Au₃₀@BSA clusters. Simple dark current-voltage traces of the solar cells are shown in Figure 6 itself which correspond to the

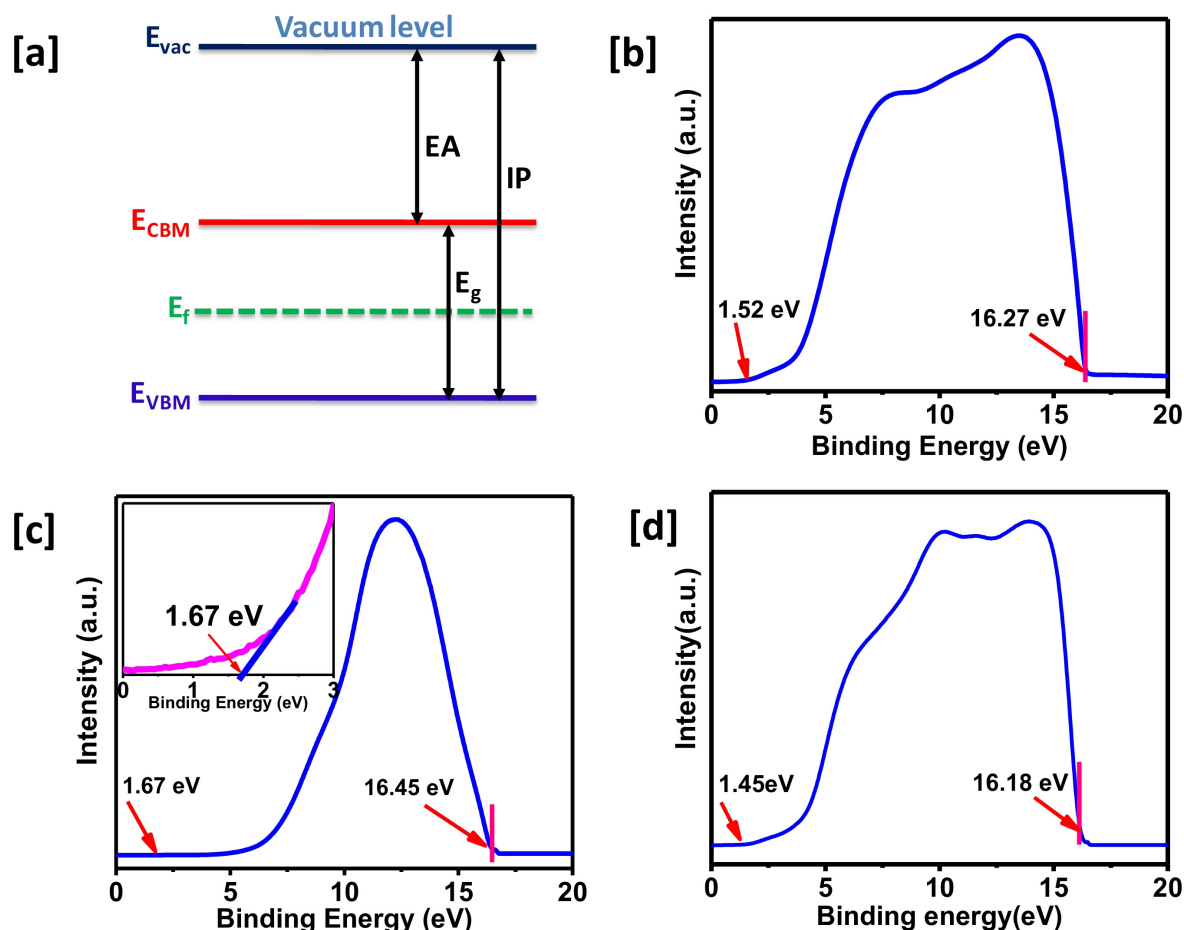


Figure 4. Energy levels diagram near the valence region [a] and typical He 1 UPS spectrum of Au₃₀BSA [b], Au₂₅SBB₁₈ (inset shows the point of maximum inflection) [c] and Ag₄₄MBA₃₀ [d].

Table 1. Photovoltaic performance of Au₂₅SBB₁₈, Ag₄₄MBA₃₀ and Au₃₀@BSA QCSSCs

Photoanode	Thickness (μm)	V _{oc} (V)	J _{sc} (mA/cm ²)	FF (%)	η (%)
Au ₂₅ SBB ₁₈					
P25	12	0.69 ± 0.11	0.42 ± 0.06	42.45 ± 8.0	0.14 ± 0.008
P25	18	0.76 ± 0.13	0.42 ± 0.03	46.70 ± 6.0	0.15 ± 0.001
NT	12	0.68 ± 0.01	0.45 ± 0.03	42.31 ± 5.0	0.13 ± 0.002
NT	18	0.74 ± 0.10	0.45 ± 0.05	44.58 ± 6.0	0.13 ± 0.006
Ag ₄₄ MBA ₃₀					
P25	12	0.64 ± 0.001	0.45 ± 0.04	52.70 ± 1.3	0.15 ± 0.004
P25	18	0.75 ± 0.06	0.36 ± 0.11	52.77 ± 2.7	0.14 ± 0.003
NT	12	0.68 ± 0.02	0.53 ± 0.04	53.30 ± 4.1	0.19 ± 0.006
NT	18	0.64 ± 0.04	0.41 ± 0.15	63.03 ± 11.1	0.16 ± 0.004
Au ₃₀ @BSA					
P25	12	0.75 ± 0.12	0.42 ± 0.07	54.34 ± 6.2	0.17 ± 0.004
P25	18	0.91 ± 0.05	0.62 ± 0.09	52.25 ± 3.1	0.30 ± 0.012
NT	12	0.86 ± 0.02	0.60 ± 0.01	46.19 ± 1.4	0.24 ± 0.004
NT	18	0.98 ± 0.011	0.71 ± 0.13	50.07 ± 7.6	0.35 ± 0.003

characteristics of diode. The corresponding J_{sc} and V_{oc} values of dark current values are tabulated in SI Table 1. Error bar graphs of short-circuit current density, J_{sc} [a], open-circuit voltage, V_{oc} [b], fill factor (FF) [c] and power conversion efficiency (PCE) (d) of Au₂₅SBB₁₈, Ag₄₄MBA₃₀ and Au₃₀@BSA clusters on P25 and TiO₂

of the TiO₂ whereas it is at the same and below, respectively, than that of TiO₂ for Au₂₅SBB₁₈ and Ag₄₄MBA₃₀. This implies that the injection of the photoexcited electrons from the LUMO of the quantum cluster to the CB of the TiO₂ is energetically favorable only in the case of Au₃₀BSA though its band-gap (1.65

NT with two different thicknesses (12 and 18 μm, respectively) are shown in Figure S10. Error bars (Figure S10) represents minimum and maximum values. It would be interesting to know why the Au₃₀@BSA system showed better photovoltaic parameters in comparison to the other two clusters despite its larger band-gap.

A possible explanation could be given based on the energy level diagram shown in Figure 5b. It is evident from Figure 5b that the LUMO level of the Au₃₀BSA cluster is positioned above the CB maximum

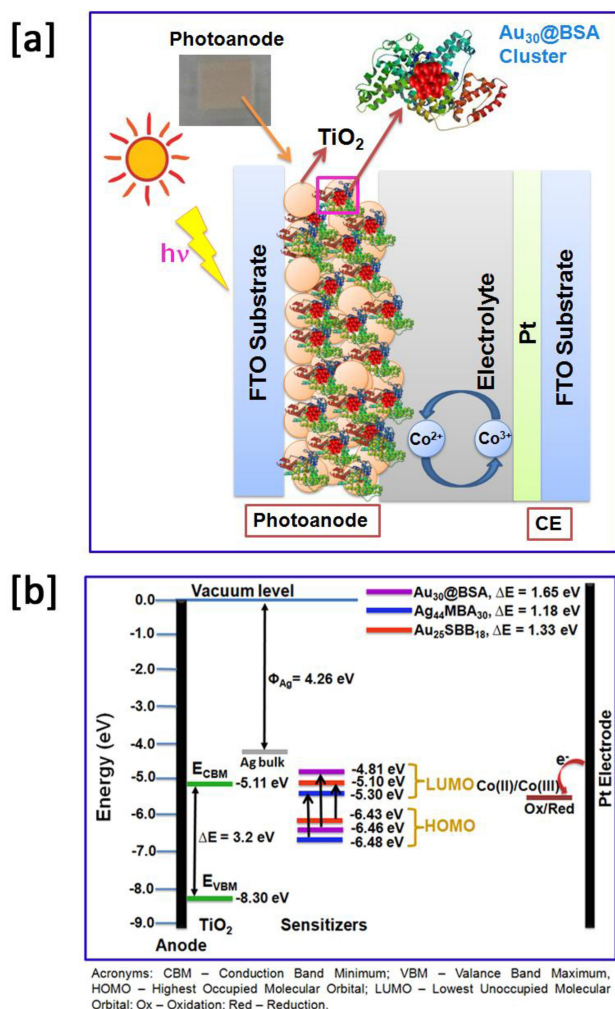


Figure 5. Schematic representation of the quantum cluster-sensitized solar cell (QCSC) [a] and schematic illustration of the relative energy levels of TiO_2 and QCs [b].

eV) is unfavorable for light absorption in comparison to the other two clusters (1.33 eV and 1.18 eV, respectively). The LUMO of the $\text{Au}_{25}\text{SBB}_{18}$ (-5.10 eV) is positioned almost at the same level as the CB of TiO_2 (-5.11 eV) and the electron transfer is less energetically favorable. The energy level alignments further imply that the photoinjected electrons are also vulnerable to back-electron transfer. These account for the lower efficiency of $\text{Au}_{25}\text{SBB}_{18}$. In the case of $\text{Ag}_{44}\text{MBA}_{30}$, the LUMO level (-5.30 eV) is positioned below the CB of the TiO_2 (-5.11 eV) thus making injection of the photoexcited electrons to the TiO_2 totally unfavorable.

It must also be noted that BSA ligands have functional groups such as $-\text{COOH}$ and $-\text{NH}_2$ ^[75] which are desired for anchoring onto the TiO_2 surfaces (with the surface $-\text{OH}$ groups) chemically which ensures a good electronic coupling between $\text{Au}_{30}\text{@BSA}$ and TiO_2 for efficient electron transfer. Though MBA also has $-\text{COOH}$ groups for efficient electronic coupling between TiO_2 and $\text{Ag}_{44}\text{@MBA}_{30}$, the electron injection is unfavorable because of the unfavorable band alignments. In

the case of $\text{Au}_{25}\text{@SBB}$, the SBB ligand being a thiol, doesn't have the desired functionalities for chemically binding to the TiO_2 . Thus the absence of a good electronic coupling between TiO_2 and $\text{Au}_{25}\text{@SBB}$ coupled with the unfavorable band-gap alignment (LUMO being at nearly the same position as that of the CB of TiO_2 and hence the back-electron transfer) results in lower efficiency for the system. Between $\text{Au}_{25}\text{SBB}_{18}$ and $\text{Ag}_{44}\text{MBA}_{30}$, the $\text{Ag}_{44}\text{MBA}_{30}$ is expected to have the lower efficiency; however, the efficiency shown by $\text{Ag}_{44}\text{MBA}_{30}$ was slightly greater than that of the $\text{Au}_{25}\text{SBB}_{18}$, which needs further investigations. Thus amongst the systems investigated, the Au_{30}BSA performed well as a sensitizer in comparison to the $\text{Au}_{25}\text{SBB}_{18}$ and $\text{Ag}_{44}\text{MBA}_{30}$. Despite the explanations based on band-gap alignments and electronic coupling, we admit that detailed investigations using open-circuit voltage decay (OCVD) and electrochemical impedance measurements are essential to understand the charge transport mechanism in cluster-sensitized solar cells. We wish to have these results as part of a future publication. It must also be mentioned that the traditional electrolytes such as the I^-/I_3^- and the Co redox couple may not be the right electrolyte systems for quantum cluster-sensitized solar cells. It is, hence, a necessity to investigate on suitable electrolytes to be used for quantum cluster sensitizers for their optimum performance.

Sakai *et al.*^[41] have used $\text{Au}_{25}\text{SG}_{18}$ as a sensitizer for solar cells and achieved an energy conversion efficiency (η) of 0.26% using the hydroquinone electrolyte. They have also reported TiO_2 loaded with glutathione-protected silver clusters (Ag_{15} , Ag_{25} and Ag_{29}) showing incident photon-to-electron conversion efficiency of 19.5%, 14.3% and 20.6%, respectively.^[48] The work concluded that Ag clusters function as photosensitizers similar to Au clusters.

The photostability of atomically precise clusters in cluster-loaded TiO_2 is of vital importance for their end use as sensitizers in solar cells. Metal clusters of different core sizes and surface passivation ligands have unique structures and distinctly different photostability parameters. It is generally observed that thiol-protected quantum clusters have reasonably good stability under long excitation times.^[76-78] However, a recent study by Liu and Xu throws light on the instability of the quantum clusters, loaded on TiO_2 electrodes.^[79] It was observed that glutathione (SG)-protected Au_{25} clusters ($(\text{Au}_{25}(\text{SG})_{18})$)-loaded TiO_2 electrodes upon irradiation with simulated solar light/visible light, undergo partial oxidative transformation to a mixture of large plasmonic nanoparticles (~ 15 nm) and quantum clusters. However, the precise factors controlling the structures and photostability of such complex material systems are still not known and hence a combined theoretical and experimental approach connecting the role of vital parameters such as geometric shell closing, electronic shell closing and surface passivation of ligands need to be considered to answer this fundamentally important question.^[80]

In 2013, Nakata *et al.*^[49] have obtained a conversion efficiency of 0.034% for the TiO_2 photoanode sensitized with both glutathione-protected Au_{25} cluster and N719 using hydroquinone electrolyte. TiO_2 electrodes sensitized with glutathione protected Au_{25} and N719 showed the conversion efficiencies of

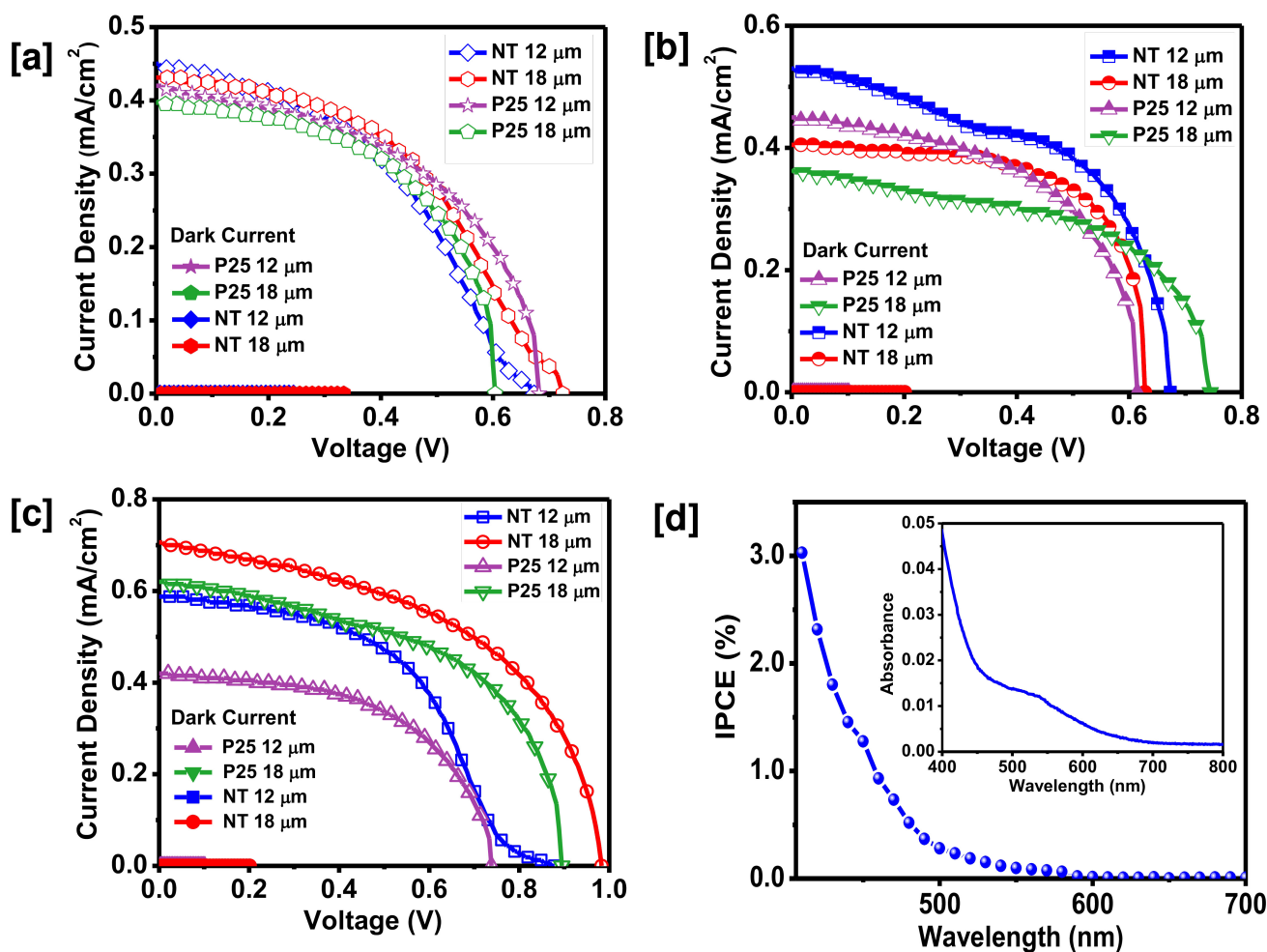


Figure 6. J-V characteristics of the QSC made out of the synthesized TiO₂NTs and commercial P25 TiO₂ sensitized with Au₂₅SBB₁₈ [a], Ag₄₄MBA₃₀ [b] and Au₃₀@BSA [c]; Corresponding dark current plots are also shown in the graphs. The IPCE spectrum of Au₃₀@BSA modified TiO₂ NT (thickness 18 μm) [d]. Inset shows the UV-vis spectrum of Au₃₀@BSA cluster.

0.005% and 0.007%, respectively. When these reports are compared with the present work, the Au₃₀@BSA-sensitized 18 μm thick TiO₂ NT and P25 cell show better efficiencies of 0.35% and 0.30%, respectively. This highlights the fact that similar systems have to be compared to get better results.

Conclusions

The utility of several quantum clusters of different types as sensitizers for TiO₂ is reported. A systematic study with various quantum clusters (Au₂₅SBB₁₈, Ag₄₄MBA₃₀ and Au₃₀@BSA) on two different TiO₂ materials showed that the protein-protected gold cluster (Au₃₀@BSA) in the QSCSSC has shown promising efficiency as a light harvesting system. The Au₃₀@BSA modified TiO₂ NTs showed energy conversion efficiency of 0.35% which is higher compared to the other clusters used for analysis. It is evident from various analyses that the Au₃₀@BSA modified TiO₂ NTs system showed better absorption of light in the visible region and has increased light scattering due to the dimensions of the NTs. Factors such as the favorable alignment of the

LUMO of the cluster to the CB of TiO₂, and the presence of –COOH groups in the ligands (which causes better electronic coupling between the orbitals of the cluster and the CB of TiO₂) were responsible for the high efficiency of the Au₃₀@BSA modified TiO₂ NTs system. This study suggests further exploration of other protein-protected clusters for solar cell applications.

Supporting Information (SI) Summary

Details on materials and methods and characterization including photoluminescence spectra of Au₃₀@BSA cluster, UV-Vis spectra of Ag₄₄MBA₃₀, histograms showing size distribution of the clusters, XPS spectrum of TiO₂ NTs, SEM image and XRD, respectively, of P25 TiO₂, TEM/EDS and Raman spectra of Au₃₀@BSA modified TiO₂, and UPS spectrum of standard polycrystalline Ag. Fabrication of solar cells with the clusters and a table showing their dark current characteristics.

Acknowledgements

We thank the Department of Science and Technology, Government of India for constantly supporting our research program on nanomaterials. We thank Anuradha Govindarajan, Jyotisarita Mohanti, Mohd Azhardin Ganayee and Radha Gobinda Bhuin for their technical supports in PL measurements, transmission electron microscopy, Raman analysis and XPS, respectively.

Conflict of Interest

The authors declare no conflict of interest.

Keywords: Nanotubes · Quantum clusters · Sensitization · Solar cells · Titanium dioxide.

- [1] M. Walter, J. Akola, O. Lopez-Acevedo, P. D. Jadzinsky, G. Calero, C. J. Ackerson, R. L. Whetten, H. Gronbeck, H. Hakkinen, *PNAS* **2008**, *105*, 9157–9162.
- [2] C. A. J. Lin, T. Y. Yang, C. H. Lee, S. H. Huang, R. A. Sperling, M. Zanella, J. K. Li, J. L. Shen, H. H. Wang, H. I. Yeh, H. Parak, W. H. Chang, *ACS Nano* **2009**, *3*, 395–401.
- [3] M. A. H. Muhammed, P. K. Verma, S. K. Pal, A. Retnakumari, M. Koyakutty, S. Nair, T. Pradeep, *Chem. Eur. J.* **2010**, *16*, 10103–10112.
- [4] A. Retnakumari, S. Setua, D. Menon, P. Ravindran, M. A. H. Muhammed, T. Pradeep, S. Nair, M. Koyakutty, *Nanotech.* **2010**, *21*, 055103–055115.
- [5] S. Liu, F. Lu, J. J. Zhu, *Chem. Commun.* **2011**, *47*, 2661–2663.
- [6] D. Son, S. Y. Park, B. Kim, J. T. Koh, T. H. Kim, S. An, D. Jang, G. T. Kim, W. Jhe, S. Hong, *ACS Nano* **2011**, *5*, 3888–3895.
- [7] H. Liu, X. Zhang, X. Wu, L. Jiang, C. Burda, J. J. Zhu, *Chem. Commun.* **2011**, *47*, 4237–4239.
- [8] B. Adhikari, A. Banerjee, *Chem. Mater.* **2010**, *22*, 4364–4371.
- [9] A. Leelavathi, T. U. B. Rao, T. Pradeep, *Nanoscale Res. Lett.* **2011**, *6*, 123–132.
- [10] K.-I. Shimizu, Y. Miyamoto, A. Satsuma, *J. Catal.* **2010**, *270*, 86–94.
- [11] H. Tsunoyama, H. Sakurai, N. Ichikuni, Y. Negishi, T. Tsukuda, *Langmuir* **2004**, *20*, 11293–11296.
- [12] H. Tsunoyama, H. Sakurai, Y. Negishi, T. Tsukuda, *J. Am. Chem. Soc.* **2005**, *127*, 9374–9375.
- [13] C. Han, N. Zhang, Y. J. Xu, *Nano Today* **2016**, *11*, 351–372.
- [14] N. Zhang, M. Q. Yang, S. Liu, Y. Sun, Y. J. Xu, *Chem. Rev.* **2015**, *115*, 10307–10377.
- [15] N. Zhang, C. Han, Y. J. Xu, J. J. Foley, D. Zhang, J. Codrington, S. K. Gray, Y. Sun, *Nature Photonics* **2016**, *10*, 473–482.
- [16] S. Yamazoe, K. Koyasu, T. Tsukuda, *Acc. Chem. Res.* **2014**, *47*, 816–824.
- [17] X. Yuan, Z. Luo, Y. Yu, Q. Yao, J. Xie, *Chem. Asian J.* **2013**, *8*, 858–871.
- [18] A. Mathew, T. Pradeep, *Part. Part. Syst. Charact.* **2014**, *31*, 1017–1053.
- [19] J. P. Wilcoxon, B. L. Abrams, *Chem. Soc. Rev.* **2006**, *35*, 1162–1194.
- [20] P. Maity, S. Xie, M. Yamauchi, T. Tsukuda, *Nanoscale* **2012**, *4*, 4027–4037.
- [21] I. Diez, M. Pusa, S. Kulmala, H. Jiang, A. Walther, A. S. Goldmann, A. H. E. Mueller, O. Ikkala, R. H. A. Ras, *Angew. Chem. Int. Ed.* **2009**, *48*, 2122–2125.
- [22] A. Tlahuice, I. L. Garzón, *Phys. Chem. Chem. Phys.* **2012**, *14*, 7321–7329.
- [23] I. R. Antoine, F. Bertorelle, M. Vojkovic, D. Rayane, E. Salmon, C. Jonin, P. Dugourd, R. Antoine, P. F. Brevet, *Nanoscale* **2014**, *6*, 13572–13578.
- [24] S. A. Khan, D. Senapati, T. Senapati, P. Bonifassi, Z. Fan, A. K. Singh, A. Neeley, G. Hill, P. C. Ray, *Chem. Phys. Lett.* **2011**, *512*, 92–95.
- [25] A. Mathew, P. R. Sajanlal, T. Pradeep, *Angew. Chem., Int. Ed.* **2012**, *51*, 9596–9600.
- [26] A. Ghosh, V. Jeseentharani, M. A. Ganayee, R. G. Hemalatha, K. Chaudhari, C. Vijayan, T. Pradeep, *Anal. Chem.* **2014**, *86*, 10996–11001.
- [27] A. Mathew, P. R. Sajanlal, T. Pradeep, *J. Mater. Chem.* **2011**, *21*, 11205–11212.
- [28] P. L. Xavier, K. Chaudhari, P. K. Verma, S. K. Pal, T. Pradeep, *Nanoscale* **2010**, *2*, 2769–2776.
- [29] S. Yang, A. Sreekumaran Nair, S. Ramakrishna, *Mater. Lett.* **2014**, *116*, 345–348.
- [30] L. Giribabu, K. Sudhakar, V. Velkannan, *Curr. Sci.* **2012**, *102*, 991–1000.
- [31] A. Connell, P. J. Holliman, E. W. Jones, L. Furnell, C. Kershaw, M. L. Davies, C. D. Gwennan, M. B. Pitak, S. J. Coles, G. Cooke, *J. Mater. Chem. A* **2015**, *3*, 2883–2894.
- [32] K. Hara, Z. S. Wang, T. Sato, A. Furube, R. Katoh, H. Sugihara, Y. D. Oh, C. Kasada, A. Shinpo, S. Suga, *J. Phys. Chem. B* **2005**, *109*, 15476–15482.
- [33] S. Ito, S. M. Zakeeruddin, R. Humphry-Baker, P. Liska, R. Charvet, P. Comte, M. K. Nazeeruddin, P. Pechy, M. Takata, H. Miura, S. Uchida, M. Grätzel, *Adv. Mater.* **2006**, *18*, 1202–1205.
- [34] X. Lu, Q. Feng, T. Lan, G. Zhou, Z.-S. Wang, *Chem. Mater.* **2012**, *24*, 3179–3187.
- [35] H. Hug, M. Bader, P. Mair, T. Glatzel, *Appl. Energy* **2014**, *115*, 216–225.
- [36] N. A. Ludin, A. M. A. Mahmoud, A. B. Mohamad, A. A. H. Kadhum, K. Sopian, N. S. A. Karim, *Renew. Sust. Energ. Rev.* **2014**, *31*, 386–396.
- [37] E. M. Barea, V. G. Pedro, T. R. Sanchis, H. P. Wu, L. L. Li, C. Y. Yeh, E. W. Diau, J. Bisquert, *J. Phys. Chem. C* **2011**, *115*, 10898–10902.
- [38] J. Luo, M. Xu, R. Li, K. W. Huang, C. Jiang, Q. Qi, W. Zeng, J. Zhang, C. Chi, P. Wang, J. Wu, *J. Am. Chem. Soc.* **2014**, *136*, 265–272.
- [39] A. Yella, H. W. Lee, H. N. Tsao, C. Yi, A. K. Chandiran, Md. Khaja Nazeeruddin, E. W. Diau, C. Yeh, S. M. Zakeeruddin, M. Grätzel, *Science* **2011**, *334*, 629–634.
- [40] B. O'Regan, M. Grätzel, *Nature* **1991**, *353*, 737–740.
- [41] N. Sakai, T. Tatsuma, *Adv. Mater.* **2010**, *22*, 3185–3188.
- [42] Z. Wu, G. Gayathri, R. R. Gil, R. Jin, *J. Am. Chem. Soc.* **2009**, *131*, 6535–6542.
- [43] M. Zhu, C. M. Aikens, M. P. Hendrich, R. Gupta, H. Qian, G. C. Schatz, R. Jin, *J. Am. Chem. Soc.* **2009**, *131*, 2490–2492.
- [44] T. Huang, R. W. Murray, *J. Phys. Chem. B* **2001**, *105*, 12498–12502.
- [45] A. Kogo, N. Sakai, T. Tatsuma, *Nanoscale* **2012**, *4*, 4217–4221.
- [46] R. N. Naphade, M. Tathavadekar, J. P. Jog, S. Agarkar, S. Ogale, *J. Mater. Chem. A* **2014**, *2*, 975–984.
- [47] S. Muduli, O. Game, V. Dhas, K. Vijayamohan, K. A. Bogle, N. Valanoor, S. B. Ogale, *Solar Energy* **2012**, *8*, 1428–1434.
- [48] N. Sakai, S. Nakamura, T. Tatsuma, *Dalton Trans.* **2013**, *42*, 16161–16165.
- [49] K. Nakata, S. Sugawara, W. Kurashige, Y. Negishi, M. Nagara, S. Uchida, C. Terashima, T. Kondo, M. Yuasa, A. Fujishima, *Int. J. Photoenergy* **2013**, *2013*, 1–7.
- [50] R. M. Barrer, *Hydrothermal Chemistry of Zeolites*, Academic Press, London, **1982**, p. 360.
- [51] J. S. Mohanty, P. L. Xavier, K. Chaudhari, M. S. Bootharaju, N. Goswami, S. K. Pal, T. Pradeep, *Nanoscale* **2012**, *4*, 4255–4262.
- [52] I. Chakraborty, W. Kurashige, K. Kanehira, L. Gell, H. Hakkinen, Y. Negishi, T. Pradeep, *J. Phys. Chem. Lett.* **2013**, *4*, 3351–3355.
- [53] M. S. Mathew, A. Bakshi, T. Pradeep, K. Joseph, *Biosens. Bioelectron.* **2016**, *81*, 68–74.
- [54] A. Mathew, E. Varghese, S. Choudhury, S. K. Pal, T. Pradeep, *Nanoscale* **2015**, *7*, 14305–14315.
- [55] J. S. Mohanty, A. Bakshi, H. Lee, T. Pradeep, *RSC Adv.* **2015**, *5*, 48039–48045.
- [56] I. Chakraborty, S. Mahata, A. Mitra, G. De, T. Pradeep, *Dalton Trans.* **2014**, *43*, 17904–17907.
- [57] E. S. Shibu, M. A. H. Muhammed, T. Tsukuda, T. Pradeep, *J. Phys. Chem. C* **2008**, *112*, 12168–12176.
- [58] Y. Negishi, K. Nobusada, T. Tsukuda, *J. Am. Chem. Soc.* **2005**, *127*, 5261–5270.
- [59] M. A. H. Muhammed, T. Pradeep, *Chem. Phys. Lett.* **2007**, *449*, 186–190.
- [60] A. Mathew, G. Natarajan, L. Lehtovaara, H. Hakkinen, R. M. Kumar, V. Subramanian, A. Jaleel, T. Pradeep, *ACS Nano* **2014**, *8*, 139–152.
- [61] A. Desireddy, B. E. Conn, B. E. J. Guo, B. Yoon, R. N. Barnett, B. M. Monahan, K. Kirschbaum, W. P. Griffith, R. L. Whetten, U. Landman, T. P. Bigioni, *Nature* **2013**, *501*, 399–402.
- [62] I. Chakraborty, J. Erusappan, A. Govindarajan, K. S. Sugi, T. Udayabhaskararao, Atanu Ghosh, T. Pradeep, *Nanoscale* **2014**, *6*, 8024–8031.
- [63] H. C. Choi, Y. M. Jung, S. B. Kim, *Vib. Spec.* **2005**, *37*, 33–38.
- [64] T. Ohsaka, *J. Phys. Soc. Jpn.* **1980**, *48*, 1661–1668.
- [65] K. R. NarendraPai, G. S. Anjusree, T. G. Deepak, D. Subash, S. V. Nair, A. S. Nair, *RSC Adv.* **2014**, *4*, 36821–36827.
- [66] J. Pan, G. Liu, G. Q. Lu, H. M. Cheng, *Angew. Chem. Int. Ed.* **2011**, *50*, 2133–2137.

- [67] D. Chu, A. Younis, S. Li, *J. Phys. D: Appl. Phys.* **2012**, *45*, 355306–355309.
- [68] M. N. Ghazzal, R. Wojcieszak, G. Raj, E. M. Gaigneaux, *Beilstein J. Nanotech.* **2014**, *5*, 68–76.
- [69] K. H. Leong, H. Y. Chu, S. Ibrahim, P. Saravanan, *Beilstein J. Nanotech.* **2015**, *6*, 428–437.
- [70] M. Chen, X. Wang, Y. H. Yu, Z. L. Pei, X. D. Bai, C. Sun, R. F. Huang, L. S. Wen, *Appl. Surf. Sci.* **2000**, *158*, 134–140.
- [71] M. Ghaffari, H. Huang, O. K. Tan, M. Shannon, *Cryst. Eng. Comm.* **2012**, *14*, 7487–7492.
- [72] Y. Park, Y. So, S. J. Chung, J. I. Jin, *J. Korean Phy. Soc.* **2000**, *37*, 59–63.
- [73] N. Yaghoobi Nia, P. Farahani, H. Sabzyan, M. Zendehtdel, M. Oftadeh, *Phys. Chem. Chem. Phys.* **2014**, *16*, 11481–11491.
- [74] M. Gratzel, *Nature* **2001**, *414*, 338–344.
- [75] J. Y. Yoon, H. Y. Park, J. H. Kim, W. S. Kim, *J. Colloid Interface Sci.* **1996**, *177*, 613–620.
- [76] Y. Changlin, G. Li, S. Kumar, H. Kawasaki, R. Jin, *J. Phys. Chem. Lett.*, **2013**, *4*, 2847–2852.
- [77] Y. S. Chen, P. Kamat, *J. Am. Chem. Soc.*, **2014**, *136*, 6075–6082.
- [78] Y. S. Chen, H. Choi, P. V. Kamat, *J. Am. Chem. Soc.*, **2013**, *135*, 8822–8825.
- [79] S. Liu, Y. J. Xu, *Scientific Reports*, **2016**, *6*, 22742–22754.
- [80] R. Jin, *Nanoscale*, **2015**, *7*, 1549–1565.

Submitted: November 10, 2016

Accepted: January 20, 2017